http://www.jgg09.com
Doi:10.3724/SP.J.1246.2010.00015

Study on crustal deformation of the *Ms*6.6 Damxung earthquake in 2008 by InSAR measurements

Xuejun Qiao, Shanjun Ren, Zhaosheng Nie, Yu Zhou, Qiang Shen and Shaomin Yang
Institute of Seismology, China Earthquake Administration, Wuhan 430071, *China*

Abstract: Three Envisat images from ESA were used to derive the pre- and co-seismic deformation interfereograms caused by the Damxung *Ms*6.6 earthquake of Oct. 6, 2008, by using InSAR. The result shows no significant crustal motion more than 4 months before the earthquake, but a maximum co-seismic displacement of about 0.3 m in an epicentral area of 20 km × 20 km. The deformation field was symmetrically distributed about a NS axis, where the west side subsided and the east side uplifted. We used a linear elastic dislocation model in half space and a nonlinear constraint optimized algorithm to estimate the slip distribution along the fault. The results indicates that the epicenter is located at 90.374°E, 29.745°N with a moment magnitude of *Mw*6.35. The earthquake is dominated by normal faulting with a maximum slip of 3 m on a 12 km × 11 km fault plane striking S189°W, dipping 60° to NW at a depth of 9.5 km, and is located at a sub-fault of the southeastern Piedmont of the Nyainqentanglha mountains. The relatively shallow depth of earthquake is related to relatively high heat flow in the area.

Key wards: InSAR(synthetic aperture radar interferometry); co-seismic deformation; Damxung; Yadong-Gulu rift; southeastern Piedmont of the Nyainqentanglha mountains

1 Geological background

An *Ms*6.6 earthquake struck Damxung in China's Tibet Autonomous region on October 6, 2008[1,2]. According to the focal mechanism solution and the field survey results, it occurred at an active fault zone southeast of the Nyainqêntanglha Mountains, and located at the west edge of Yangbajing-Damxung graben in the north-central section of Yadong-Gulu rift, which is a late-Cenozoic crustal extension structure 120 km long and 10 – 25 km wide. The southeastern foothill of Nyainqêntanglha mountain fault zones strike mostly to NE, and partly to EW; mainly distributed in the northwest of the basin, partly inside the basin at the east edge(Fig. 1)[3,4]. The basin-border fault, which was very active in Quaternary, is a seismically active belt within the plateau. For example, an *Ms*8.0 earthquake occurred in 1411 and another *Ms*7.5 occurred in 1952, both at Damxung[6,7]. Therefore, by determining the distribution and structure characteristics of the fault, we can not only explain the seismic movement and dynamic process, but also help to study the evolution and movement characters of southern Tibetan Plateau graben at a typical mountain – basin fault belt. Previous investigations of the southern section of the fault zone are limited to seismo-geological studies, but studies on earthquake distribution and characteristics are inadequate. In order to better understand the earthquake focal mechanism, time-space distribution of deformation and the structural characteristics of the seismogenic fault, we obtained surface deformation images related to the

Received:2010-09-11; Accepted: 2010-10-15
Corresponding author. Tel. +86 -027 - 87863562; E-mail: xuejunq@sohu.com
This study is supported by the National Natural Science Fundation of China(40774014, 40674054, 40575011, 40674009)

Damxung earthquake by using synthetic aperture radar interferometry (InSAR), inversed the epicentral depth and slip distribution along the fault plane, and analyzed the structure characteristics of the epicenter area from the contemporary deformation point of view.

2 InSAR data and processing

The InSAR observation can provide earth-surface displacement images in all kinds of weather condition at a centimeter-level accuracy and and a spatial resolution of tens of meters[8,9]. It has been widely used since the 1990s in earthquake and crustal deformation studies[9-13].

We obtained three images on 4th May, 21st September and 26th October 2008 from ESA satellite Envisat-1 for the present study (tab. 1). The first two images, obtained before the earthquake, can be used to detect pre-earthquake crustal deformation, which can then be matched with the third image, which was captured after the earthquake, to obtain the co-seismic deformation field. Envisat-1 satellite used C-band observations and the 3-view low-pass images. The satellite orbit information is mainly based on the precise orbit which was determined by Doirs positioning system and released by the European Space Agency.

The JPL developed ROI_PAC 3.0 software was used for processing the raw data. The SRTM digital elevation model (DEM) released by NASA was used to eliminate the topographic effect. The spatial resolution of this model was 3 s, and the horizontal and vertical accuracy were 20 m and 16 m, respectively[14]. For phase unwrapping we used Stanford University's statistics cost

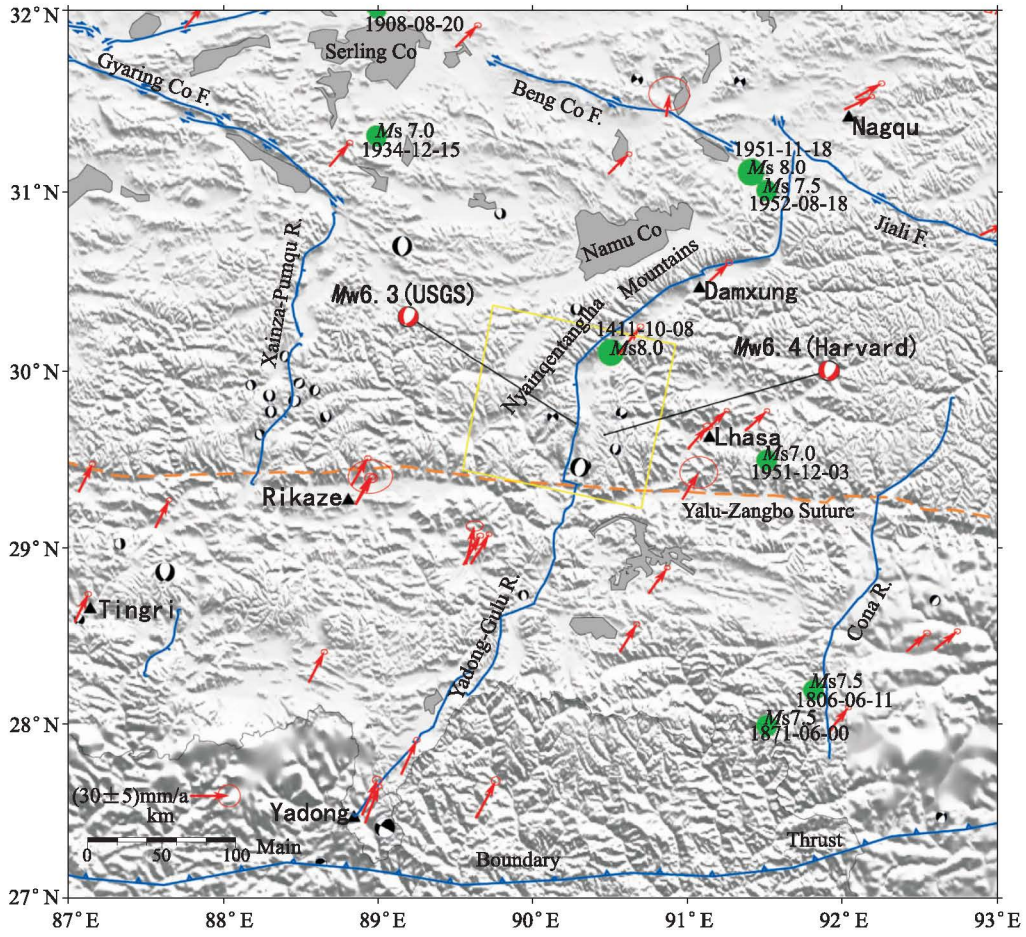

Figure 1 Regional topography, active tectonics, earthquake epicenter, GPS velocity field and InSAR measurements in the study area. Red arrows show GPS speed field; beach balls are focal mechanism solutions provided by Harvard University; black-white balls are $Mw \geqslant 5.0$ earthquake between 1976-2008; red-white balls are Damxung focal mechanisms released respectively by USGS and Harvard University; green dots are historical $Ms \geqslant 7.0$ strong earthquakes; blue lines are active fault zones and rift valley zones; half arrows accompanied by solid line, triangular spikes and short branches are strike-slip, thrust and normal fault, respectively; orange dotted line is a structure seam; and pink quadrangle is the SAR observation area. Topographic data are from SRTM digital elevation model.

Table 1 Information of SAR image

No.	Date of acquisition	Track	Frame	Orbit	$B_\perp$ (m)	Interval (days)
IP1	2008-05-04-2008-09-21	176	3007	32294/34298	171	140
IP2	2008-05-04-2008-10-26	176	3007	32294/34799	-52	175
IP3	2008-09-21-2008-10-26	176	3007	34298/34799	-223	35

network flow algorithm program SNAPHU[15], which is based on statistical methods using maximum posterior probability to solve the optimum phase ambiguity; it can accomplish the whole interferogram phase unwrapping.

The InSAR ranging errors come mainly from atmospheric delay and DEM and orbital errors. Of these three, the water vapor caused atmosphere delay has the largest effect. However, in the Qinghai-Tibet Plateau, which has an average elevation of 5000 m, the average error caused by water vapor variation is less than 1 mm/a, due to the high altitude, dry climate, and relatively low total content of water vapor[16]. In addition, if using shorter vertical baseline for the Doris orbit, the effect of DEM error on the ranging can be reduced also[19,20]. The ranging accuracy can be 5 -10 cm[17,18]. According to a formula derived in the literature[17], the vertical baselines of the three pairs of images we use are 171 m, -52 m and -233 m, respectively. When the accuracy of SRTM DEM is 25 m, the ranging errors are 1.3 cm, 0.4 cm and 1.7 cm, respectively.

3 Deformation and fault displacement by inversion

The final data obtained by InSAR represent distance changes between a ground point and the satellite along the line of sight (LOS); a positive value indicates subsidence and a negative value, uplift. IP1 is an interference image obtained 140 days before the earthquake (Fig. 2). The LOS changes are mostly within the range of -1 - 1 cm, which is smaller than the estimated DEM observation error of 1.3 cm, which means no pre-earthquake deformation was detected in the epicentral area. IP2 and IP3 are interference images showing significant co-seismic deformation (Fig. 3 and 4), with LOS changes of -7.19 -27.56 cm and -9.35 - 27.53 cm, respectively. In order to further reduce the orbit and atmospheric-delay errors, we superposed the two interferograms to obtain a composite co-seismic deformation field of Damxung earthquake (Fig. 5). This interferogram shows two northwest-southeast parallel quasi-concentric rings. The upper left ring (left plate) represents a surface subsidence area, located in Jidaguo basin, where the fringes in the interferogram are more continuous, clear, with good resolution on the eastern side, but are less coherent on the the west side close to the Nyainqentanglha Mountains. The lower right ring (right plate) represents an uplift zone located at a terrace on the eastern boundary of the basin, and the image is not very clear. The subsidence area is larger than the uplift area, and they can be divided by an approximately N9° E trending axis (Fig. 5). The subsidence center obtained is located near 90.377°E and 29.743° N, which agrees well with the result of a field survey, which shows a location at Yang Yi village of Damxung Geda Township (90.40°E, 29.715°N). By moving the axis OO' up and down across the earthquake zone, we got 3 parallel profile lines to show the sight displacement (Fig. 5). The maximum subsidence and uplift are 27.3 cm and 6.5 cm, respectively, the difference being 33.8 cm. Assuming that all co-seismic deformation of the surface was due to vertical displacement, then the maximum relative vertical variation calculated by InSAR is 37 cm.

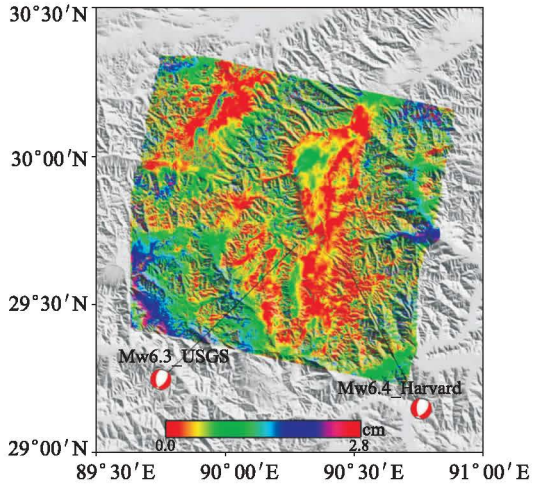

Figure 2 Pre-seismic interferogram from IP1 SAR pair

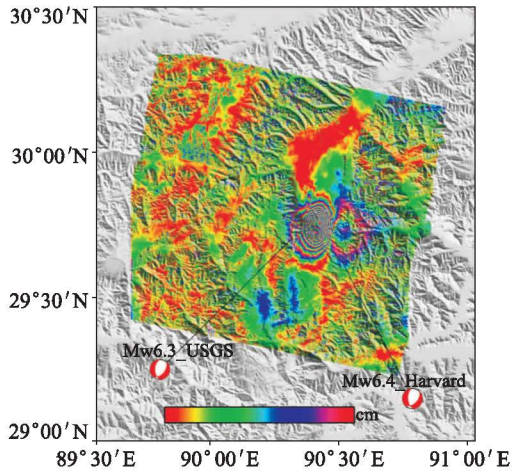

Figure 3 Co-seismic interferogram from IP2 SAR pair

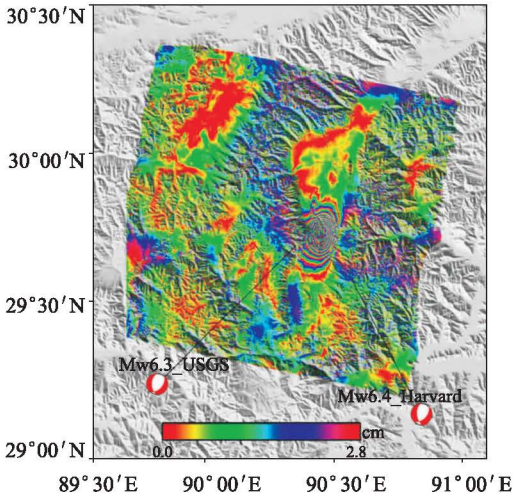

Figure 4 Co-seismic interferogram from IP3 SAR pair

Based on the symmetry of the quasi-concentric rings in the co-seismic interference image and the asymmetry in the amount of surface deformation, together with the CMT focal mechanism solution, we attribute the Damxung earthquake to primarily a normal faulting.

We used Okada's elastic half-space homogeneous dislocation theory[21] with a constrained nonlinear optimization algorithm[22] to divide the main active fault into several small fault elements, and InSAR co-seismic deformation field to calculate the fault dimension and offset distribution. Our calculations was based on a CMT focal mechanism solution, ignoring the strike-slip along the fault, and setting the slip angle orthogonal with the strike.

Assuming that the surface displacement of InSAR observation is d and the amount of dislocation is s, then their relationship can be expressed as:

$$d = G(m) + s + \varepsilon \tag{1}$$

$G(m)$ is the Green function related to fault, including fault trend, dip, depth, position, length, width, etc, and ε is the observation error. We divided the fault plane into a number of fault elements, and inversed the offset of each element from equation (1). To ensure that dislocations of different elements have continuous smooth variations and to avoid inconsistent dislocation directions of elements, the simulated values and InSAR observations must meet the following conditions:

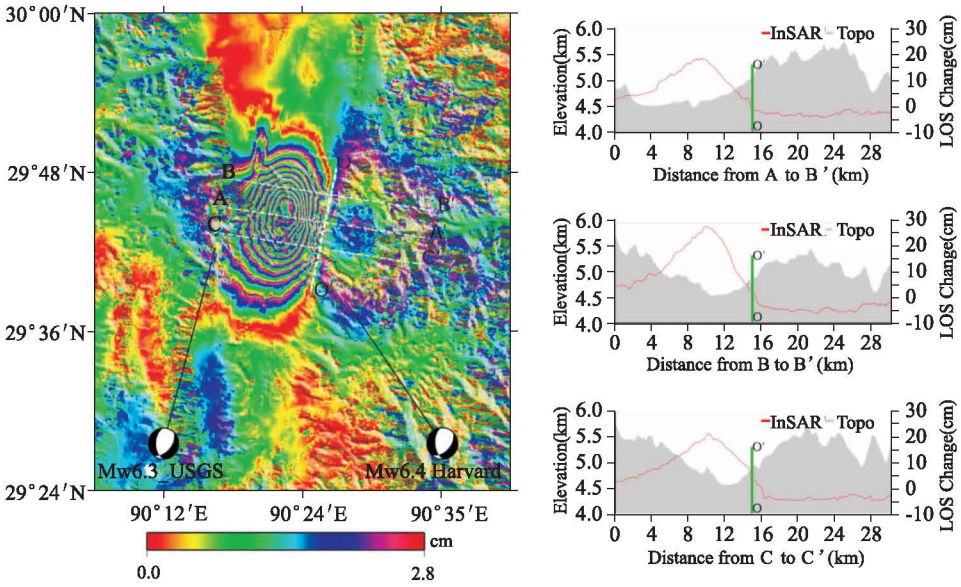

Figure 5 Composite co-seismic interferogram of pair IP2 and IP3. Here OO' is the border between subsidence and uplift parts, AA', BB', and CC' are displacement profile lines across the earthquake zone, shades of gray in the right image indicates the terrain.

$$\min [\| G(m)s - d \|^2 + \beta^2 \| \nabla^2 s \|^2] \quad (2)$$

In this equation, $\|\|^2$ is the Euclidean norm, $G(m)s-d$ is the residual, β is the factor to control the smooth degree of fault and the coincident extent of fault dislocation, ∇^2 is the Laplacian for constraint smoothing degree of the fault.

In the simulation calculation, we first use the CMT solution of Harvard and USGS as the initial reference models. By adjusting the width, length, location of the fault and dislocation parameter we conducted a series of forward calculations. Under the condition that the seismic moment[5] (shear modulus 33GP) is generally consistent with the CMT result, we finally selected a set of best fault parameters as input for the nonlinear optimization algorithm, and constrained the fault trend, dip, depth, position, length, and width, and estimated the offset of the fault. The results are shown in Figure 6-7 and Table 2. The overall residual of the fit is less than 1 cm; the maximum residual is less than 4 cm.

In this result, the epicenter is located at 90.374° E, 29.745° N, the dislocation occurred in a depth range of 5.2° 14.8 km, the focal depth is 9.5 km, the fault plane is 12 km wide, 11 km long, striking S189° W, dipping 60°, the maximum offset of the fault plane is 3 m, the seismic moment is 4.07×10^{18} Nm. The moment magnitude is *Mw*6.35, which is between the magnitudes given by USGS and Harvard.

4 Discussion

Damxung earthquake occurred in the southeastern Piedmont of the Nyainqentanglha Mountains at a fault about 250 km long, which is the tectonic, geomorphological and stratigraphic boundary of the northeastern Tibet. The fault was very active during the Quaternary period, and is a controlling factor[23] of plateau topography, tectonic block motion and the distribution of strong earthquakes, etc. Geological survey shows that the southern section of the fault zone begins at Longbanongbu in the north and ends at Xumai in the south; its trend is NNW to NS and total length is 50 km (Fig. 8), formed by 3 sub-faults and dominated by a right-lateral normal fault fracture.

Table 2 Comparison between different focal mechanism soluction of the Dumxung *Ms*6.6 earthquake

Model	Epicenter	Depth (km)	Strike (°)	Dip (°)	Slip angle (°)	Seismic Moment (Nm)	Slip (m)	Width (km)	Length (km)
USGS *Mw*6.3	90.274°E,29.704°N	10.0	40/180	50/48	-60/-119	3.4×10^{18}	N/A	N/A	N/A
Hravad *Mw*6.4	90.46°E,29.66°N	12.0	44/175	49/53	-53/-125	4.3×10^{18}	N/A	N/A	N/A
This study *Mw*6.35	90.374°E,29.754°N	9.5	189	60	-90	4.07×10^{18}	0-3	12	11

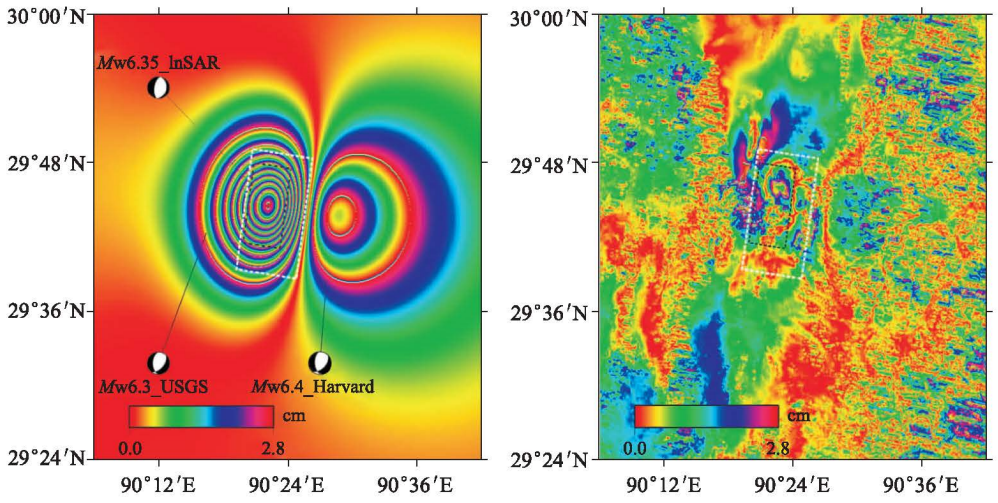

Figure 6 Simulated interferogram and residual (Black and white dashed rectangular square boxes show, respectively, the dislocation fault plane and the fault model's projection at the surface)

The InSAR result shows that the earthquake did not occur at the main fault, but at an eastern sub-fault, which is the boundary of southeastern edge of the Jidaguo basin (Fig. 8). The distribution characteristic of fault dislocation (Fig. 7) shows no obvious dislocation from the surface to a depth of 5.2 km. But field investigation found some feather-shaped columns of surface ruptures along a highway. This may be just a local phenomenon caused by strong earthquake shaking. The observed high-angle normal faulting movements shows that the southern section of the Yangbajin-Damxung rift basin is mainly under east-west tension.

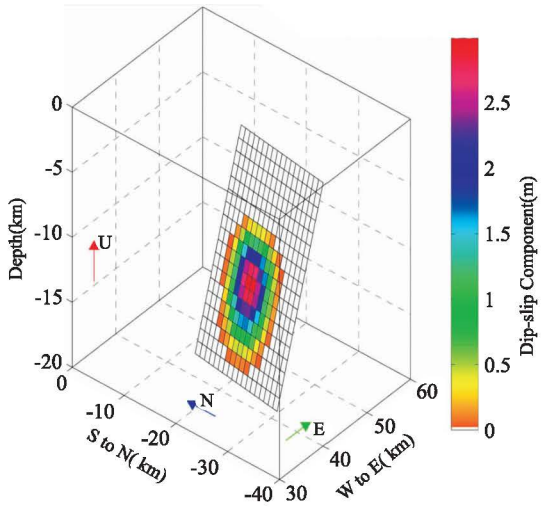

Figure 7 Estimated fault model and slip distribution for the Damxung earthquake

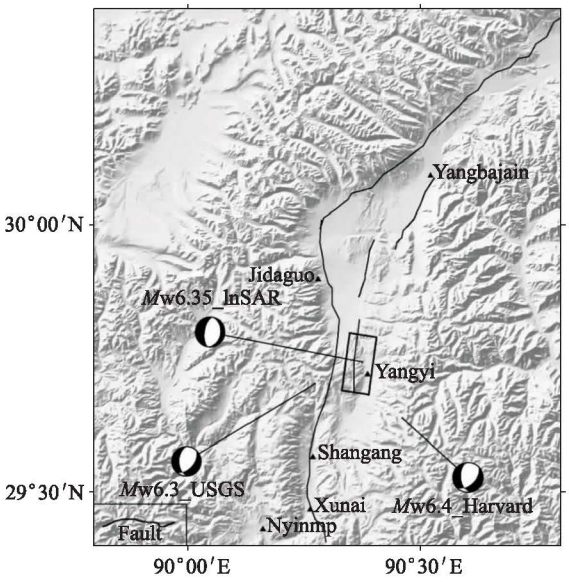

Figure 8 Focal mechanism solutions and geological structure (F1-F3 are the northern, central and southern segments of the southeastern Piedmount of the Nyainqentanglha Mountains)

The average crustal thickness of Qinghai-Tibet Plateau is 60-80 km, and the average focal depth of earthquakes is 33 ± 12 km[24], but the focal depth of the Damxung earthquake estimated in our study is only 9.5 km. This shallow depth may be related to the high heat flow in the epicentral area, for when the crust temperature is higher, the depth of aseismic layer is shallower[25-27]. The heat flow values observed in Yang Yi Village, Prado Kong and other areas are unusually high, reaching 364 mW/m^2[28-39].

The epicenter determined in our study is different from those of Harvard and USGS by 14 km and 10 km, respectively (Fig. 8), but is close (less than 3 km different) to that of a preliminary field investigation-located at Geda Township Yang Yi Village (90.40° E, 29.72°N). Due to the sparsity of stations in the Qinghai-Tibet seismic station network, earthquake location and fault plane solutions are determined mainly on the basis of teleseismic data, which limits the positioning accuracy[25,31], So, the application of InSAR to the study of earthquake location, focal mechanism and rupture is quite essential in the Qinghai-Tibet region. Damxung earthquake caused the epicenter region to sink by 10 cm (Fig. 5) in the northwest direction on the average. Comparing with the maximum basin undulation of about 500 m, the present basin structure can be formed by about 5000 earthquakes of comparable magnitude, inspite of surface erosion. If the graben were entirely the result of earthquake ruptures like the Damxung earthquake occurring every 600 to 800 years, then the Jidaguo basin would have a development history of about 300 to 400 thousands years.

5 Conclusions

The pre- and co-seismic deformations and the interference images of the Damxung earthquake, based on the ESA Envisat-1 radar remote sensing data, indicated that the epicentral area did not show any significant crustal deformation more than 4 months before the earthquake, but showed a co-seismic crustal deformation of 0.34 m concentrated in a 20 km × 20 km area, having maximum values symmetrically distributed about a north-south axial, with the western part descending and the eastern uplifting. By using a homogeneous elastic half-

space dislocation model and constrained nonlinear optimization algorithm, we found the earthquake to be a normal rapture with epicenter at 90.374°E, 29.745°N, which is close to the location of a preliminary field investigation——Geda Township Yang Yi Village (90.40° E, 29.72° N); the maximum dislocation of fault plane is 3 m, the seismic moment is 4.07×10^{18} Nm, and the corresponding magnitude is *Mw*6.35, in agreement with the results published by USGS and Harvard. The earthquake did not occur at the main fault of the southeastern Piedmont of the Nyainqentanglha Mountains, but at a sub-fault of the southern section (striking S189°W, dipping 60° to NW). The causative fault plane is 12 km wide, 11 km long, and 9.5 m deep. This study also shows that InSAR, like GPS, can be used to study the position, focal mechanism, and failure mode of earthquakes, and the change of the structure of the Qinghai-Tibet Plateau.

Acknowledgments

We are grateful to the ESA for providing Envisat images(C1P.5070). We thank two reviewers and the editor for their helpful comments to improve our manuscript.

References

[1] http://www.globalcmt.org/CMTsearch.html.

[2] http://neic.usgs.gov/neis/eq_depot/2008/eq_081006_xva9/neic_xva9_cmt.html.

[3] Wu Zhangming, et al. Primary research on the Nianqing Tanggula Mountain southeastern pediment fault. Journal of Seismological Research, 1990, 13(1):40-50.

[4] He Rizheng, Gao Rui. Some significances of studying north-southern rift in Tibet plateau. Progress in Geophysics, 2003, 18(1):35-43.

[5] Wu Zhonghai, et al. Study of Quaternary geology and faulting of Damxung-yang bajain basin. Journal of Geomechanics, 2006, 12(3):205-315.

[6] Wu Zhenhan, et al. Slip rates and driving mechanism of active faults in middle Tibetan plateau. Acta Geosicientia Sinica, 2005, 26(2):99-104.

[7] Chen Zhengwei, et al. Study of Quaternary activity features of the Yadong-Gulu tectonic belt based on the digital elevation model. Earthquake, 2004, 24(s1):41-46.

[8] Wu Zhenhan, et al. Album of active faults and geological hazards along the Golmud-Lhasa railway across the Tibetan plateau. Beijing: Seismological Publishing House, 2005. (in Chinese).

[9] Institute and of Geology, CEA Active faults in the central Tibet. Beijing: Seismological Press. (in Chinese).

[10] Armijo R, et al. Quaternary extension in Southern Tibet: Field observations and tectonic implications. J. Geophys. Res., 1986, 91: 13803-13872.

[11] Armijo R, Tapponnier P and Han T L. Late Cenozoic right-lateral strike-slip faulting in southern Tibet. J. Geophys. Res., 1989, 94: 2787-2838.

[12] Molnar P and Tapponnier P. Active tectonics of Tibet. J. Geophys. Res., 1978, 83:5361-5375.

[13] Tapponnier P, et al. Oblique stepwise rise and growth of the Tibet. Science, 2001, 294:1671-1677.

[14] Chen Zhengwei, et al. Activity of the Ningjinkangsha west piedmont fault in southern Tibet in later Quaternary. Progress in Geophysics, 2006, 1:118-126.

[15] Zhang P-Z, et al. Continuous deformation of the Tibetan plateau from Global Positioning System data. Geology, 2004, 32:809-812.

[16] Wang Q, et al. Present-day crustal deformation in China constrained by Global Positioning System measurements. Science, 2001, 294:574-577.

[17] Deng Qidong, China active tectonic map(1:4000000). Beijing: Seismological Press, 2007. (in Chinese)

[18] Taylor M and Peltzer G.. Current slip rates on conjugate strike slip faults in Central Tibet using Synthetic Aperture Radar Interferometry. J. Geophys. Res., 2006, 111, B12402, doi: 10.1029/2005JB004014.

[19] Massonnet D, et al. The displacement field of the Landers earthquake mapped by radar interferometry. Nature, 1993, 364: 138-142.

[20] Massonnet D and Feigl K. Radar interferometry and its application to changes in the Earth's surface. Rev Geophys., 1998, 36:441-500.

[21] Sun Jianbao, et al. InSAR deformation observation and preliminary analysis of the *Ms*8.0 Wenchuan earthquake. Seismology and Geology, 2008, 30(3):789-795. (in Chinese)

[22] Salichon J, et al. Slip history of the 1999 16 October *Mw* 7.1 Hector Mine earthquake(California) from the inversion of InSAR, GPS, and teleseismic data. Bull. Seism. Soc. Am., 2004, 94: 2015-2027.

[23] Cakir Z, et al. Coseismic and early post-seismic slip associated with the 1999 Izmit earthquake(Turkey), from SAR interferometry and tectonic field observations. Geophys. J. Int., 2003, 155: 93-110.

[24] Meyer B, Armijo R and Massonetr D. The 1995 Grevena(Northern Greece) earthquake fault model constrained with tectonic observations and SAR interferometry. Geophys. Res. Lett., 1996, 23: 2677-2680.

[25] Fialko Y, et al. Three-dimensional deformation caused by the Bam, Iran, earthquake and the origin of shallow slip deficit. Nature, 2005, 435:295-299.

[26] Peltzer G., Crampe F and King G. Evidence of nonlinear elasticity of the crust from the *Mw*7.6 Manyi(Tibet) earthquake. Science, 1999, 286:272-276.

[27] Farr T, et al. The shuttle radar topography mission. Rev. Geophys., 2007, 45: RG2005, doi: 10.1029/2005RG000172.

[28] Chen C and Zebker H. Network approaches to two-dimensional phase unwrapping: intractability and two new algorithms. J. Opt. Soc. Am., 2000, 17:401-414.

[29] Wright T, Parsons B and England P. InSAR observations of low slip rates on the major faults of western Tibet. Science, 2004, 305:236-239.

[30] Cazenave A and Valette C. Positioning results with DORIS on

SPOT2 after first year of mission. Geophys. Res. Lett., 1992: 7109-7119.

[31] Scharroo R and Visser P. Precise orbit determination and gravity field improvement for the ERS satellites. J. Geophys. Res., 1998, 103:8113-8127.

[32] Simons M, Fialko Y and Rivera L. Coseismic deformation from the 1999 *Mw*7.1 Hector Mine, California, earthquake as inferred from InSAR and GPS observations. Bull. Seismol. Soc. Am., 2002, 92: 1390-1402.

[33] Li Zhenghong, Liu Jingnan and Xu Caijun, Error analysis in In-SAR data processing. Geomatics and Information Science of Wuhan University, 2004, 29(1):72-76. (in Chinese)

[34] Fialko Y. Interseismic strain accumulation and the earthquake potential on the southern San Andreas fault system. Nature, 2006, 441:968-971.

[35] Okada Y. Surface deformation due to shear and tensile faults in a half-space. Bull. Seismol. Soc. Am., 1985, 75:1135-1154.

[36] Bürgmann R, et al. Postseismic strain following the 1989 Loma Prieta earthquake from GPS and leveling measurements. J. Geophys. Res. 1997, 102:4933-4955.

[37] Kanamori H. The energy release in great earthquakes. J. Geophys. Res., 1977, 82:2981-2987.

[38] Chen W P and Molnar P. Focal depths of intracontinental and intraplate earthquake and their implication for the thermal and mechanical properties of the lithosphere. Journal of Geophysical Research, 1983, 88(B5):4183-4214.

[39] Bai Jiaqi, Mei Ling and Yang Meiling. Geothermal resources and crustal thermal structure of the Qinghai-Tibet pleteau. Journal of Geomechanics, 2006, 12(3):354-362.